RESEARCH ARTICLE

Dynamic wind loads and wake characteristics of a wind turbine model in an atmospheric boundary layer wind

Hui Hu · Zifeng Yang · Partha Sarkar

Abstract An experimental study was conducted to characterize the dynamic wind loads and evolution of the unsteady vortex and turbulent flow structures in the near wake of a horizontal axis wind turbine model placed in an atmospheric boundary layer wind tunnel. In addition to measuring dynamic wind loads (i.e., aerodynamic forces and bending moments) acting on the wind turbine model by using a high-sensitive force-moment sensor unit, a high-resolution digital particle image velocimetry (PIV) system was used to achieve flow field measurements to quantify the characteristics of the turbulent vortex flow in the near wake of the wind turbine model. Besides conducting "free-run" PIV measurements to determine the ensemble-averaged statistics of the flow quantities such as mean velocity, Reynolds stress, and turbulence kinetic energy (TKE) distributions in the wake flow, "phase-locked" PIV measurements were also performed to elucidate further details about evolution of the unsteady vortex structures in the wake flow in relation to the position of the rotating turbine blades. The effects of the tip-speed-ratio of the wind turbine model on the dynamic wind loads and wake flow characteristics were quantified in the terms of the variations of the aerodynamic thrust and bending moment coefficients of the wind turbine model, the evolution of the helical tip vortices and the unsteady vortices shedding from the blade roots and turbine nacelle, the deceleration of the incoming airflows after passing the rotation disk of the turbine blades, the TKE and Reynolds stress distributions in the near wake of the wind turbine model. The detailed flow field measurements were correlated with the dynamic wind load measurements to elucidate underlying physics in order to gain further insight into the characteristics of the dynamic wind loads and turbulent vortex flows in the wakes of wind turbines for the optimal design of the wind turbines operating in atmospheric boundary layer winds.

1 Introduction

With the oil and gas supply security and climate change emerging as high concerns, the need for renewable energy sources to alleviate dependence on hydrocarbons and reduce carbon dioxide (CO_2) emissions is becoming increasingly urgent. Wind energy is one of the cleanest renewable power sources in the world today. While wind energy provided only approximately 1.0% of total U.S. electricity generation in 2008, a target of 20% of USA total electricity generation from wind energy by 2030 has been set up recently by the U.S. Department of Energy. To achieve the goal of 20% of electricity generation by 2030, the total wind power capacity in USA will need to exceed 300 gigawatts (Schreck et al. 2008). Suppose if each wind turbine could generate about 2.0 MW, which corresponds to the large wind turbines with the hub height about 80 m and rotor blade diameters about 80–100 m, it would require at least 150,000 additional large wind turbines installed in onshore or/and offshore wind farms in order to meet the 20% electricity generation goal. Wind turbine dynamics, micrositing, and array effects have been identified the most significant research topics needed for wind resource characterization and wind power generation (Schreck et al.

H. Hu (✉) · Z. Yang · P. Sarkar
Department of Aerospace Engineering, Iowa State University,
2271 Howe Hall, Room 1200, Ames, IA 50010, USA
e-mail: huhui@iastate.edu

Present Address:
Z. Yang
Department of Mechanical and Materials Engineering,
Wright State University, Dayton, OH, USA

2008). More specifically, detailed measurements and modeling to characterize the surface wind energy resources and turbulent wake flows of wind turbines are highly desirable in order to provide more accurate estimations of the power generation and fatigue wind loads for the optimal design of the wind turbines.

As described in the review article of Vermeer et al. (2003), the wake of a wind turbine is typically divided into a near and a far wake. The near wake refers to the region from the turbine to approximately one rotor diameter downstream. In the near wake, the presence of the rotor is apparent by the number of blades, blade aerodynamics such as attached or stalled flows, 3-D effects, and tip vortices. A significant feature in the near wake of a wind turbine is the helical tip vortices induced by the rotating blades. The evolution of helical tip vortices has been found to affect the behavior of the turbulent wake flow structures behind a wind turbine significantly. The tip vortices were also recognized as an important source of noise generation and blade vibration (Massouh and Dobrev 2007). The far wake is the region beyond the near wake, where the actual rotor shape is less important. The main attentions to far wake flows are usually drawn in wake models, wake interference, turbulence models, and topographical effects.

A good physical understanding about the characteristics of the turbulent vortex flows in the wakes of wind turbines and the resultant dynamic wind loads acting on the wind turbines is essential for the optimal design of the wind turbines. This requires a detailed knowledge about the dynamic wind loads and transient behavior of the unsteady vortex and turbulent flow structures in the wakes of wind turbines. Although a number of experimental studies have been conducted recently to investigate wind turbine wake aerodynamics, most of the previous studies were performed based on qualitative flow visualization and/or using pointwise flow measurement techniques, such as hot-wire anemometry, hot-film anemometry, and laser Doppler velocimetry, to conduct flow velocity measurements at limited points of interest (Alfredsson and Dahlberg 1979; Tsustui and Matsumya 1987; Ebert and Wood 1997; Vermeer 2001; Medici and Alfredsson 2006; Chamorro and Porte-Agel 2009). A common shortcoming of such pointwise flow measurements is the incapability of providing spatial correlation of the turbulent vortex structures to effectively reveal the transient behavior of the unsteady vortex structures in the wake flows. Temporally synchronized and spatially resolved flow field measurements are highly desirable in order to elucidate the underlying physics to improve our understanding about the characteristics of the turbulent vortex structures in wakes of wind turbines. Contemporary flow diagnostic techniques, such as particle image velocimetry (PIV) to be used in the present study, are capable of providing such information.

Surprisingly, only very few experimental studies were conducted recently to provide flow field measurements to quantify the transient behavior of the unsteady vortex structures in the wakes of wind turbines. Whale et al. (2000) studied the tip vortices generated by an untwisted two-bladed rotor in a water tank by using a PIV system. Based on the comparison of the PIV measurements with the numerical simulation results using a rotor vortex lattice method, they reported a good qualitative agreement between the wake structures obtained from the PIV measurements and the numerical simulations, particularly in regard to the shape of the wake boundary, including features such as wake expansion and contraction, despite the difference in Reynolds numbers of the experiments and numerical simulations. They also suggested that "…the fundamental behavior of the helical tip vortices would be almost insensitive to the blade chord Reynolds number as long as the similarity of the tip-speed-ratio (TSR) of the wind turbine is observed". Grant and Parkin (2000) used a digital PIV system to measure the flow velocity fields downstream of a two-bladed wind turbine model in a low-speed wind tunnel. The PIV measurements reveal clear pictures of the turbine wake flows, including the size and persistence of the velocity deficit and tip vortices in the wake as well as the wake deflection in yaw, both aligned into the incoming wind direction and at a range of yaw angles, up to approximately 5 rotor diameters downstream. More recently, Massouh and Dobrev (2007) conducted a wind tunnel study to characterize the wake flow downstream of a small wind turbine model based on phase-locked PIV and hotwire measurements. The evolution of the helical tip vortices downstream of the wind turbine model was revealed clearly from the measurement results. While useful information has been uncovered by those previous studies, it should be noted that most of those experimental studies were conducted with the wind turbine models installed in air or water flows with homogenous, uniform incoming flow velocity, and relatively low turbulence intensity levels. However, in reality, most of the wind turbines operate in atmospheric boundary layer winds with significant variations in both mean wind speed and turbulence intensity levels along vertical directions. The effects of the significant variations in both the mean wind speed and turbulence intensity levels of the atmospheric boundary layer winds on the dynamic wind loads and the evolution of the unsteady vortex and turbulent flow structures in the wakes of wind turbines have not been fully explored.

In the present study, an experimental study was conducted to characterize the dynamic wind loads and evolution of the unsteady vortex structures in the near wake of a horizontal axis wind turbine (HAWT) model installed in an atmospheric boundary layer wind. The experimental study was performed in a large-scale aerodynamic/atmospheric

boundary layer (AABL) Wind Tunnel available at Iowa State University. In addition to measuring dynamic wind loads acting on the wind turbine model by using a high-sensitive force-moment sensor unit, a high-resolution PIV system was used to make both "free-run" and "phase-locked" PIV measurements to quantify the transient behavior of the unsteady vortex and turbulent flow structures in the near wake of the wind turbine model. The detailed flow field measurements were correlated with the dynamic wind load measurements to elucidate the underlying physics in order to gain further insight into the characteristics of the dynamic wind loads and turbulent vortex flows in the wakes of wind turbines for the optimal design of the wind turbines operating in atmospheric boundary layer winds.

2 Experimental setup and wind turbine model

2.1 Atmospheric boundary layer wind tunnel

Wind tunnel facilities have been widely used for wind turbine studies due to their capabilities to produce well-controlled flow environments. In the present study, a large-scale AABL wind tunnel located at the Aerospace Engineering Department of Iowa State University was used to perform the experimental investigations. The AABL wind tunnel is a closed-circuit wind tunnel with a test section of 20 m long, 2.4 m wide, and 2.3 m high, optically transparent side walls, and a capacity of generating a maximum wind speed of 45 m/s in the test section.

Figure 1 shows a picture of the test section of the AABL wind tunnel with a three-blade, HAWT model (at a scale ratio of 1:350) mounted in the center of a turn-table. Spike structures and arrays of wood blocks were installed at the upstream of the wind turbine model in order to generate a turbulent boundary layer flow to simulate the atmospheric
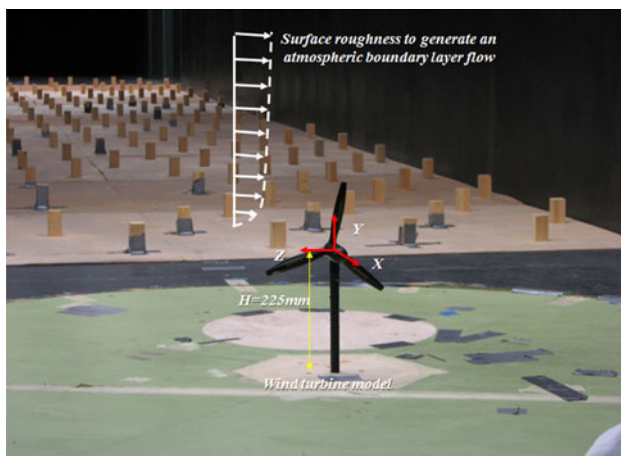

Fig. 1 A picture of the test section of the AABL wind tunnel

boundary layer winds usually seen in wind farms. Figure 2 shows the measured mean velocity and turbulence intensity profiles at the center of the turn-table, i.e., the location where the wind turbine model would be installed, by using a hotwire anemometer probe. It is well known that the wind speed at the elevation height of 10 m above the ground is widely used to characterize atmospheric boundary layer winds. The horizontal axis in Fig. 2a represents non-dimensional mean velocity $U/U(z_{10})$, where $U(z_{10})$ is the reference velocity at a height of $z_{10} = 28.6$ mm above the floor of the AABL tunnel, which is equivalent 10 m elevation height above the ground in a wind farm based on the scale ratio of 1:350. It has been suggested that the mean velocity profile of an atmospheric boundary layer flow over an open terrain can usually be fitted well by using a logarithmic function or a power function (Jain 2007), therefore, the logarithmic and power curves fitting to the measurement data were also given in Fig. 2a for comparison. It can be seen clearly that the measurement data can by represented reasonably well by either the logarithmic function or the power function. It should also be noted that, while the power law exponent for an atmospheric boundary layer wind over an open terrain in nature usually ranges from 0.1 to 0.2 according to ASCE standard (ASCE 2005), the power law exponent of the curve fitting to the present measurement data was found to be 0.165, which is well within the range of those of an atmospheric boundary layer wind over an open terrain. Figure 2b shows measured turbulence intensity of the turbulent boundary layer flow generated inside the AABL tunnel as a function of the height above the floor of the AABL tunnel. The standard turbulence intensity profile of an atmospheric boundary layer wind over an open terrain as suggested by Architectural Institute of Japan (AIJ 1996) was also plotted in the figure for comparison. It can be seen clearly that the turbulent boundary layer flow generated inside the AABL tunnel can be used to simulate the atmospheric boundary layer wind over an open terrain in nature reasonably well.

2.2 The tested wind turbine model

The wind turbine model used for the present study represents the most widely used three-blade horizontal axial wind turbines (HAWT) found in on-shore and off-shore wind farms. As shown in Fig. 3, the rotor radius of the wind turbine model is 127 mm and the height of the turbine nacelle is 225 mm above the wind tunnel floor. With the scale ratio of 1:350, the test model would represent a wind turbine in a wind farm with the rotor diameter about 90 m and tower height about 80 m. It should be noted that the blockage ratio of the wind turbine model (i.e., the ratio of the turbine blade swept area to the cross-section area of the AABL tunnel) was found to be about 1.2%. Thus, the block

Fig. 2 The measured profiles of the simulated atmospheric boundary layer wind. **a** Mean velocity profile. **b** Turbulence intensity profile
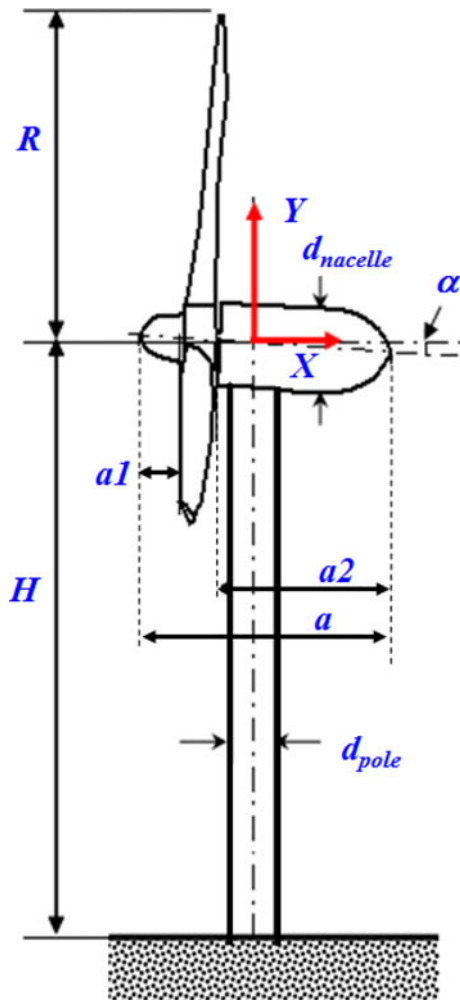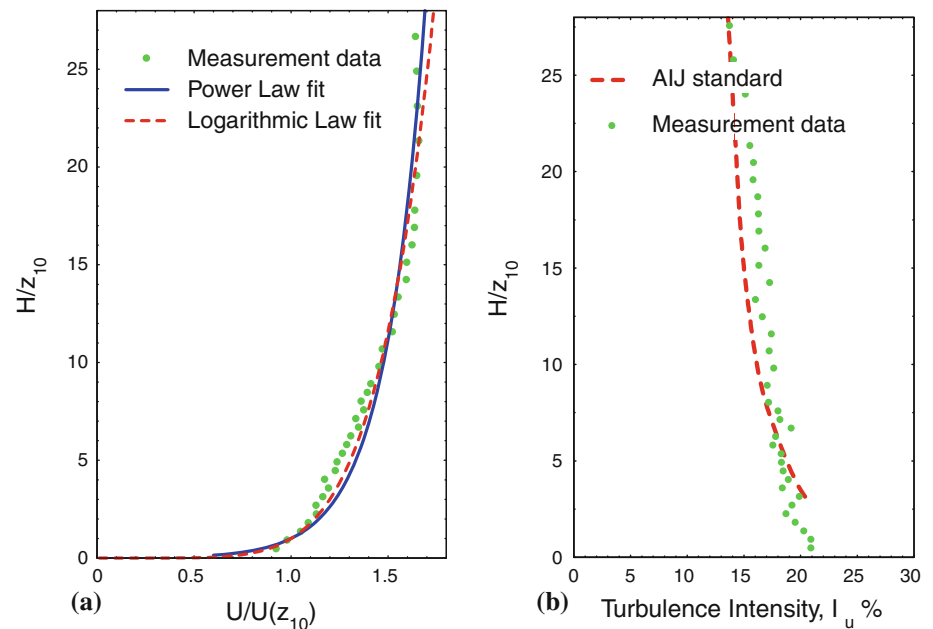

(a)

(b)

Fig. 3 A schematic of the wind turbine model used in the present study

effects of the wind turbine model would be very small, which is almost negligible, for the present study.

The rotor blades of the wind turbine model used in the present study are MA0530TE blades (Windsor Propeller Inc.), which are twisted blades with the pitch angle ranging from 20° at the root to 10° at the tip of the blades. The blades have a chord length of 12 mm at tip, 19 mm in the middle, and 16 mm at root. The airfoil cross-section of blades has a concave pressure surface and is well adapted for low Reynolds number applications. Since they were originally designed for propeller applications, the blades were mounted reversely with the pressure side of the blades facing the incoming airflow during the experiments in order to improve their aerodynamic performance when used as wind turbine blades. A small electricity generator was installed inside the nacelle of the wind turbine model, which would produce electricity as driven by the rotating blades. The primary design parameters of the wind turbine model are listed in Table 1.

During the experiments, while the wind turbine model was installed in the simulated atmospheric boundary layer wind, the mean wind speed at the hub height of the wind turbine model was set to be 4.0 m/s (i.e., $V_o = 4.0$ m/s). The corresponding chord Reynolds number (i.e., based on the averaged chord length of the rotor blades and the wind speed at hub height) was found to be about 6,000, which is significantly lower than those of the wind turbines in wind farms. It should be noted, according to Alfredsson et al. (1982), the chord Reynolds number would have significant effects on the characteristics of wind turbine performance. For example, the maximum power coefficient would be much lower for the wind turbine models operating at much

Table 1 The primary design parameters of the wind turbine model

Parameter	R	H	d_{rod}	$d_{naccele}$	α	a	$a1$	$a2$
Dimension (mm)	127	225	18	28	6°	100	15	70

lower Reynolds numbers. However, as suggested by Medici and Alfredsson (2006), the behaviors of the unsteady vortex and turbulent flow structures in the wake of wind turbines would be almost independent to the chord Reynolds numbers of the wind turbines. The wind turbines with similar tip-speed-ratio (TSR) would produce very similar near wake characteristics such as helical shape, rotation direction, and strength decay of the tip vortices.

In the present study, while the incoming atmospheric boundary layer wind was kept constant during the experiments, the rotating speed of the turbine blades was adjusted by applying different electric loads to the small electricity generator installed inside the turbine nacelle. With the rotation speed of the wind turbine blades changed from 0 to 1,700 rpm, the corresponding tip-speed-ratio of the wind turbine model (i.e., $\lambda = (\Omega R)/V_o$, where Ω is the angular speed of rotation, R is the radius of the rotor blades, and V_o is the wind speed at the hub height) was found to be changed from 0.0 to about 4.5 for the present study. It should be noted that a typical three-bladed HAWT on a wind farm usually has a tip-speed-ratio of $\lambda = 4$–6.

2.3 Experimental setup for dynamic wind load and flow field measurements

In the present study, an aluminum rod was used as the turbine tower to support the nacelle and the rotor blades of the wind turbine model. Through a hole on the wind tunnel floor, the aluminum rod was connected to a high-sensitivity force-moment sensor (JR3, model 30E12A-I40) to measure the dynamic wind loads (both aerodynamic forces and bending moments) acting on the wind turbine model. The JR3 load cell is composed of foil strain gage bridges, which are capable of measuring the forces on three orthogonal axes, and the moment (torque) about each axis. The precision of the force-moment sensor cell for force measurements is $\pm 0.25\%$ of the full range (40 N). While the force-moment sensor mounted at the bottom of the turbine tower can provide time-resolved measurements of all three components of the aerodynamic forces and the moment (torque) about each axis, only the measured thrust coefficient, C_T, and bending moment, C_{M_z}, are presented in the present study. The thrust coefficient (i.e., aerodynamic force coefficients along X-direction as shown in Fig. 4) and bending moment coefficient (i.e., the moment coefficient along Z-direction) were defined by using the expressions of

$C_T = \frac{T}{\frac{1}{2}\rho V_0^2 \pi R^2}$, and $C_{M_z} = \frac{M_z}{\frac{1}{2}\rho V_0^2 \pi R^2 H}$, where ρ is the air density, V_0 is the mean wind speed at the hub height, H. During the experiments, the wind load data were acquired for 60 s at the sample rate of 1,000 Hz for each tested case.

In addition to the wind load measurements, a high-resolution digital PIV system was used to achieve detailed flow field measurements to quantify the characteristics of the turbulent vortex flow in the wake of the wind turbine model. Figure 4 shows the schematic of the PIV system used in the present study. For the PIV measurements, the airflow was seeded with $\sim 1\ \mu m$ oil droplets by using a droplet generator. Illumination was provided by a double-pulsed Nd:YAG laser (NewWave Gemini 200) adjusted on the second harmonic and emitting two pulses of 200 mJ at the wavelength of 532 nm. The laser beam was shaped to a sheet by a set of mirrors along with spherical and cylindrical lenses. The thickness of the laser sheet in the measurement region was about 1.5 mm. A high-resolution 12-bit CCD camera (PCO2000, CookeCorp) was used for PIV image acquisition with the axis of the camera perpendicular to the laser sheet. The CCD camera and the double-pulsed Nd:YAG lasers were connected to a workstation (host computer) via a digital delay generator (Berkeley Nucleonics, Model 565), which controlled the timing of the laser illumination and the image acquisition.

After PIV image acquisition, instantaneous PIV velocity vectors were obtained by a frame to frame cross-correlation technique involving successive frames of patterns of particle images in an interrogation window of 32×32 pixels. An effective overlap of 50% of the interrogation windows was employed in PIV image processing. After the instantaneous velocity vectors (u_i, v_i) were determined, the vorticity (ω_z) can be derived. The distributions of the ensemble-averaged flow quantities such as the mean velocity, normalized Reynolds Stress $\left(\overline{\tau} = -\overline{u'v'}/U_\infty^2\right)$, and turbulence kinetic energy $\left(\text{TKE} = 0.5 \times \left(\overline{u'^2} + \overline{v'^2}\right)\Big/U_\infty^2\right)$ were obtained from a cinema sequence of about 1,000 frames of instantaneous PIV measurements. The measurement uncertainty level for the velocity vectors is estimated to be within 2%, while the uncertainties for the measurements of ensemble-averaged flow quantities such as Reynolds stress and TKE distributions about 5%.

In the present study, both "free-run" and "phase-locked" PIV measurements were performed during the

Fig. 4 Experimental setup for the dynamic wind load and PIV measurements
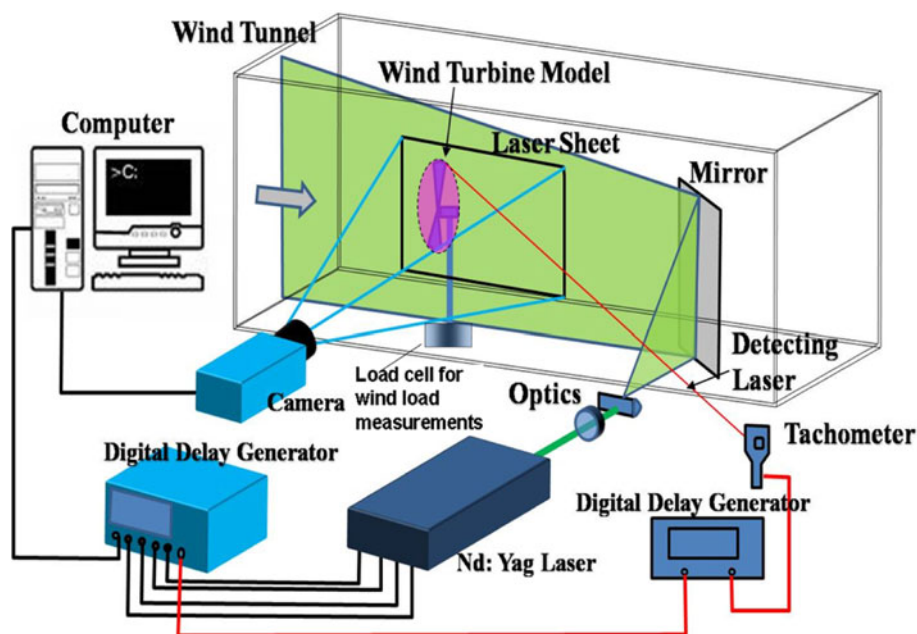
experiments. The "free-run" PIV measurements were conducted in order to determine the ensemble-averaged flow statistics (e.g., mean velocity, Reynolds Stress, and TKE) in the near wake of the wind turbine model. For the "free-run" PIV measurements, the image acquisition rate was pre-selected at a frequency that is not a harmonic frequency of the rotating frequency of the turbine rotor blades in order to ensure physically meaningful measurements of the ensemble-averaged flow quantities.

"Phase-locked" PIV measurements were also conducted in the present study in order to elucidate more details about the evolution of unsteady vortex structures in the wake of the wind turbine model in relation to the position of the rotating rotor blades. As shown in Fig. 4, a digital tachometer was used to detect the position of a pre-marked rotor blade in order to perform the "phase-locked" PIV measurements. The tachometer would generate a pulsed signal as the pre-marked rotor blade passed through the vertical PIV measurement plane. The pulsed signal was then used as the input signal to a digital delay generator (DDG) to trigger the digital PIV system for the "phase-locked" PIV measurements. By adding different time delays between the input signal from the tachometer and the TTL signal output from the DDG to trigger the digital PIV system, the "phase-locked" PIV measurements at different rotation phase angles of the pre-marked rotor blade can be accomplished. At each pre-selected phase angle (i.e., corresponding to different positions of the pre-marked rotor blade related to the vertical PIV measurement plane), 160 frames of instantaneous PIV measurements were used to calculate the phase-averaged flow velocity distribution in the wake of the wind turbine model.

3 Results and discussions

3.1 Dynamic wind load measurement results

Figure 5 shows the typical measurement results of the dynamical wind loads acting on the wind turbine model in the terms of thrust coefficient C_T and bending moment coefficient C_{M_z} with wind turbine operating at the tip-speed-ratio of $\lambda = 3.0$. As shown clearly in Fig. 5a, b, the instantaneous wind loads (both thrust and bending moment) acting on the wind turbine model were found to be highly unsteady with their magnitudes fluctuating significantly as a function of time. The time-averaged values of the measured thrust and bending moment coefficients were also plotted in the graphs as the dashed lines for comparison. It should be noted that, while time-averaged wind loads were traditionally used for the mechanical design of wind turbines, the effects of the unsteady turbulence flow and associated dynamic wind loads are paid more and more attention in recent years for optimal design of modern wind turbines. The measurement results given in Fig. 5a, b reveal clearly that the instantaneous wind loads acting on a wind turbine operating in a turbulent atmospheric boundary layer wind could be significant compared with the time-averaged values (i.e., about 2–3 times higher). The quantitative measurement results of the present study highlight the importance of taking the dynamic fluctuations of the wind loads into account for the mechanical design of wind turbines in order to improve the fatigue lifetime of wind turbines operating in turbulent atmospheric boundary layer winds.

Figure 5c, d shows the histograms of the measured dynamic thrust and bending moment acting on the wind

Fig. 5 Measured wind loads acting on the wind turbine model at $\lambda = 3.0$. **a** Time sequence of the measured C_T. **b** Time sequence of the measured C_{M_z}. **c** Histogram of the measured C_T. **d** Histogram of the measured C_{M_z}. **e** Power spectrum of measured C_T. **f** Power spectrum of measured C_{M_z}
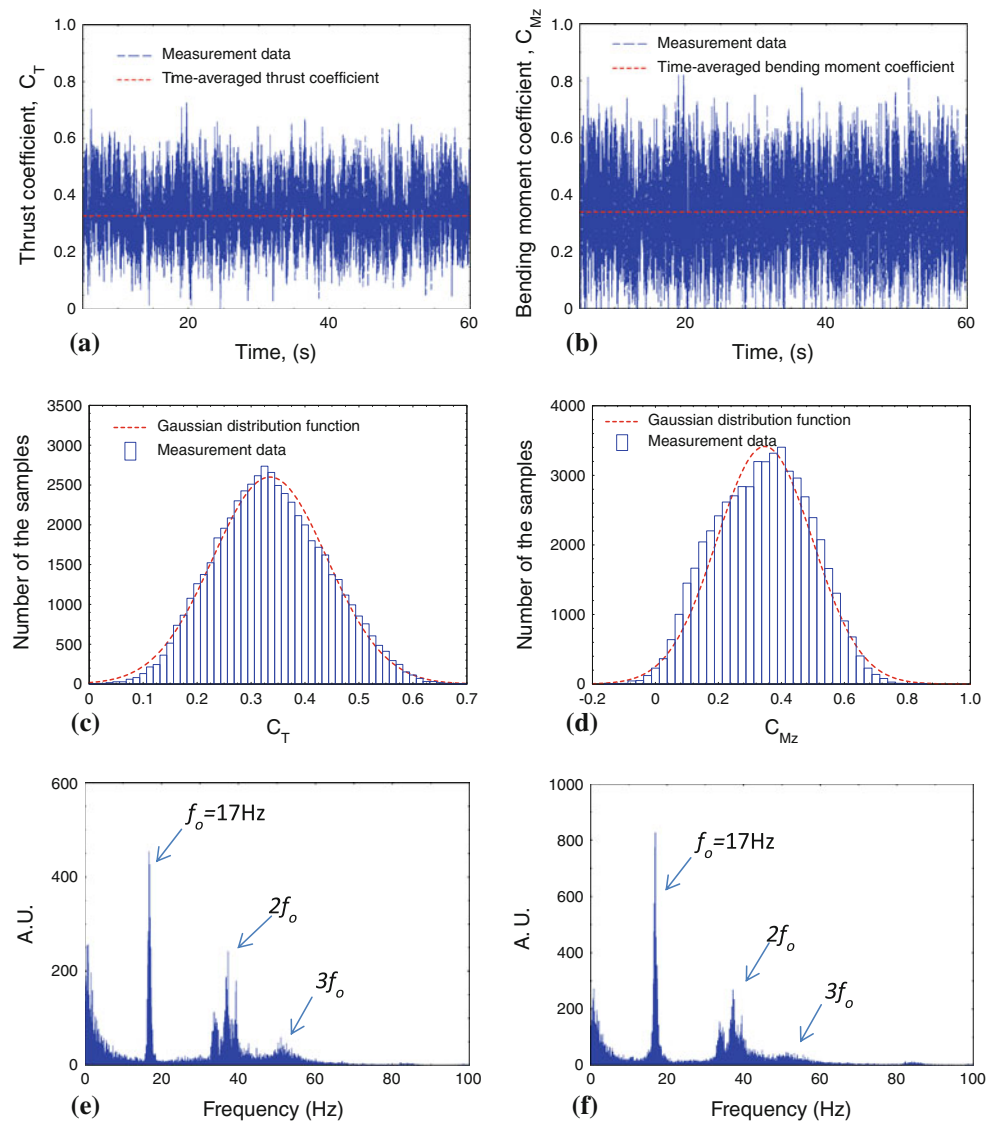
turbine model. While the instantaneous wind loads acting on the wind turbine model were found to be highly unsteady with their magnitude fluctuating randomly, the histograms of the measured aerodynamic thrust and bending moment coefficients were found to be fitted reasonably well by using Gaussian functions. While the standard deviation of the aerodynamic thrust coefficient was found to be 0.11 with the mean value at $C_T = 0.31$, the standard deviation of the bending moment coefficient was 0.15 with the mean value of $C_M = 0.35$. Figure 5e, f shows the power spectrum of the measured aerodynamic thrust and bending moment obtained through a fast Fourier transform (FFT) analysis procedure. A dominant peak at $f_0 = 17.0$ Hz can be identified in the spectrum plots, which corresponds to the rotation speed of the rotor blades of the wind turbine model at the tip-speed-ratio of $\lambda = 3.0$. The rotation frequency of $f_0 = 17.0$ Hz based on the FFT analysis of the wind load measurements was found to agree

well with the independently measured rotation speed of the rotor blades by using a tachometer. Other peaks, which represent the harmonic frequencies of the rotation frequency of the turbine rotor blades, f_0, can also be identified clearly from the power spectrum plots.

It is well known that the tip-speed-ratio (often known as TSR) of a wind turbine is of vital importance in the design of wind turbines. In the present study, the effects of the tip-speed-ratio of the wind turbine on the dynamic wind loads and the flow characteristics in the wake of the wind turbine model were investigated systematically. As described above, during the experiments, while the incoming atmospheric boundary layer wind was kept constant, the rotating speed of the rotor blades of the wind turbine model was adjusted by applying different electric loads to the small electricity generator mounted inside the turbine nacelle. It should be noted that, while the variations of the power output coefficient as a function of the tip-speed-ratio of a

wind turbine have been reported in previous studies (Boeing 1982; Jain 2007), very little can be found in the literature about the variations of the wind loads (e.g., aerodynamic thrust and bending moment) acting on wind turbines as a function of the tip-speed-ratio of the wind turbines, even though wind load data are very critical for the mechanical design of wind turbines operating in turbulent atmospheric boundary layer winds.

Figure 6 gives the measured mean thrust, C_T, and bending moment coefficient, C_M, of the wind turbine model as a function of the tip-speed-ratio of the wind turbine model, λ. The profiles of the mean thrust and bending moment coefficients were found to follow a similar trend as the tip-speed-ratio of the wind turbine model increases. As shown in the figure, the mean thrust and bending moment coefficients were found to increase gradually as the tip-speed-ratio increases while the tip-speed-ratio, λ, is still relatively small (i.e., $\lambda < 3.0$). They were found to reach their peak values at the tip-speed-ratio of $\lambda \approx 3.0$, then, began to decrease with the increasing tip-speed-ratio when the tip-speed-ratio becomes relatively big (i.e., $\lambda > 3.5$). Similar trends were also reported by Boeing (1982) and Jain (2007) to investigate the variations of the power coefficients of wind turbines as a function of the tip-speed-ratio.

The variations of the resultant flow velocity and effective angle of attack of the incoming airflow related to the turbine blade at different tip-speed-ratios may be used to qualitatively explain certain aspects of the experimental observation described above. Figure 7 shows the schematic of the flow velocity vectors relative to the cross-section of a turbine blade at different tip-speed-ratios. As shown in the figure, the magnitude of the resultant velocity of the airflow related to the turbine blade, V_{total}, and the effective angle of attack of the resultant velocity, α_{eff}, would change significantly as the tip-speed-ratio of the wind turbine model increases. The lift and drag forces acting on the turbine blade were used to deduce a resultant aerodynamic force, which is indicated by the dashed black vector in the figures. While the projection of the resultant aerodynamic force

along the direction normal to the rotation disk of the wind turbine (i.e., along X-axis direction) was measured as the aerodynamic thrust in the present study, the projection of the resultant aerodynamic force within the rotation disk of the wind turbine would be the force to drive the turbine blade rotating continuously.

As shown clearly in Fig. 7a, when the tip-speed-ratio of the wind turbine is relatively small, the resultant velocity, V_{total}, would be relatively small, while the effective angle of attack of the resultant velocity related to the turbine blade would be quite high. Airfoil stall could be expected at the high effective angle of attack, and large-scale flow separation would take place over the suction side of the turbine blade. Due to the airfoil stall along with the small resultant flow velocity, the resultant aerodynamic force acting on the turbine blade would be quite small when the tip-speed-ratio of the wind turbine is relatively small. As a result, the aerodynamic thrust force acting on the turbine blade would be small at relatively small tip-speed-ratio of the wind turbine, which was confirmed by the wind load measurements shown in Fig. 6. Spera (1994) also suggested that the performance of a wind turbine will be mainly controlled by the blade stall when the tip-speed-ratio of the wind turbine is relatively small.

As the tip-speed-ratio of the wind turbine increases, the magnitude of the resultant velocity, V_{total}, would increase, while the effective angle of attack of the airflow related to the turbine blade, α_{eff}, would decrease continuously. In an optimal operating condition, a favorable effective angle of attack will be achieved right before the occurrence of airfoil stall. As shown in Fig. 7b, a significant resultant aerodynamic force would be generated due to the favorable effective angle of attack and the larger resultant flow velocity related to the turbine blade. As a result, the aerodynamic thrust acting on the wind turbine model, which is the projection of the resultant aerodynamic force along the direction normal to the rotation disk of the wind turbine, would reach its peak value as the wind turbine operating at the optimum tip-speed-ratio ($\lambda \approx 3.0$ for the present study as shown in Fig. 6).

Fig. 6 Variations of the time-averaged wind loads as a function of the tip-speed-ratio. **a** Time-averaged thrust coefficient. **b** Time-averaged moment coefficient
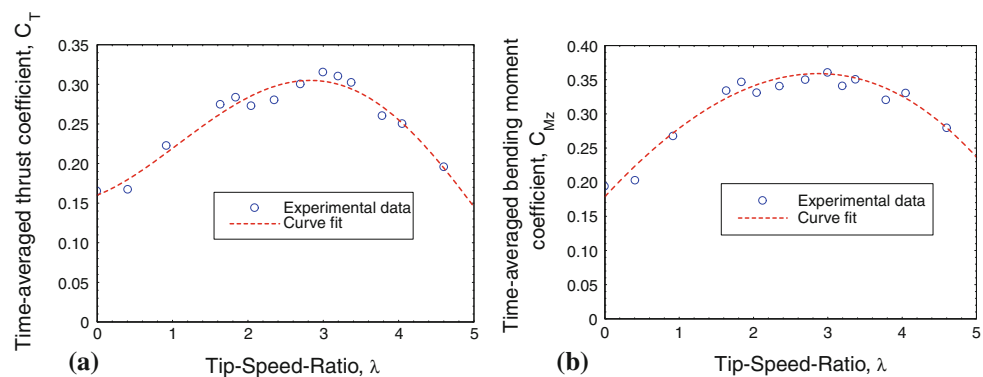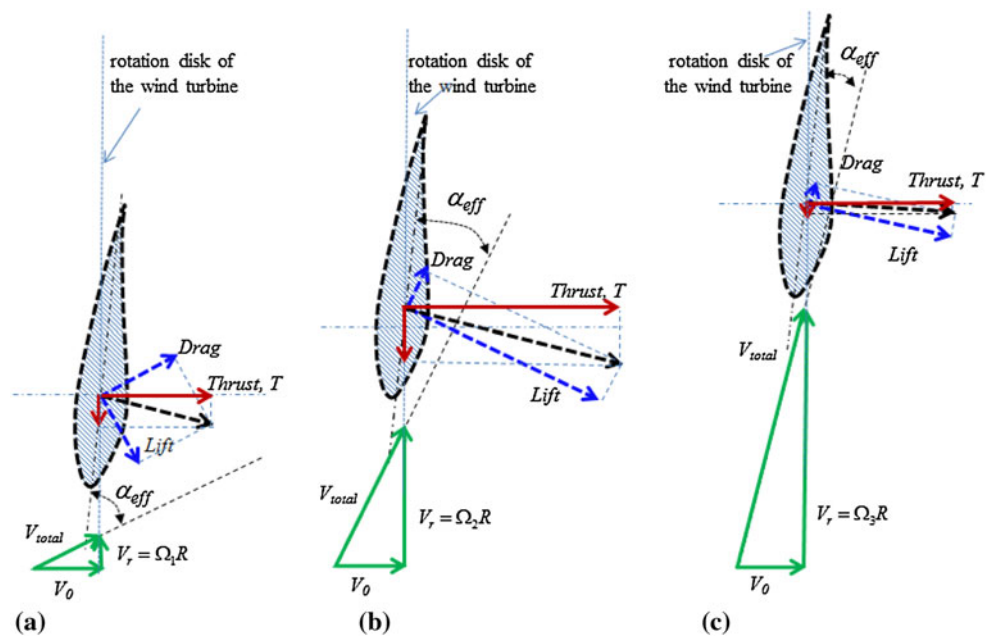
Fig. 7 Schematic of the flow velocity vectors relative to the cross-section of the turbine blade at different tip-speed-ratios. **a** The tip-speed-ratio is too small. **b** Optimal tip-speed-ratio. **c** The tip-speed-ratio is too big

As the tip-speed-ratio of the turbine blades keeps on increasing, the effective angle of attack of the airflow velocity with respect to the turbine blade would become smaller and smaller. As a result, the resultant aerodynamic force acting on the blade could become quite small, as shown in Fig. 7c. This would result in the decreasing trend of the measured aerodynamic thrust coefficient for cases with relatively big tip-speed-ratios, as revealed at the right-hand side of the profile shown in Fig. 6.

3.2 "Free-run" PIV measurement results

As described above, the flow field in the vertical plane passing the rotation axis of the wind turbine was measured by using a high-resolution PIV system. Figure 8 shows typical "free-run" PIV measurement results with the tip-speed-ratio of the wind turbine model at $\lambda \approx 3.0$. As expected, a row of tip vortex structures, which aligned themselves well in the downstream of the tips of the turbine blades, were revealed clearly from the instantaneous PIV measurement result given in Fig. 8a. A large flow separation zone can be found downstream of the turbine nacelle with its size being much greater than the diameter of the nacelle body. A series of vortex structures shedding periodically from the roots of the rotating turbine blades can also be found at the external boundary of the separation zone surrounding the turbine nacelle. The existence of the root vortex structures was also reported by Massouh and Dobrev (2007). It should also be noted that, additional flow structures were found to appear at the inboard of the blades tips at approximately 50–60% span in the form of concentrated vortex structures in the wake region. The vortex

structures were found to move outward under the influence of wake expansion as they travel downstream, and finally merging with the tip vortex structures at approximately $2.0R$ downstream. A similar flow feature was also reported by Whale et al. (2000).

As shown clearly in the ensemble-averaged PIV measurement result given in Fig. 8b, the incoming airflow was found to slow down greatly as it flows across the rotation disk of the turbine blades. Obvious velocity deficits (i.e., local wind speed is much lower than that of the incoming airflow) can be observed in the region downstream of the rotation disk of the turbine blades. It indicates that a portion of the kinetic energy of the airflow associated with the velocity deficits has been harvested by the wind turbine and turned into electric power through the electric generator inside the turbine nacelle. The expansion of the wake flow downstream of the wind turbine can be seen clearly from the distribution pattern of the iso-velocity contour lines shown in Fig. 8b. As expected, a recirculation region with much lower velocity (i.e., larger velocity deficits) was found in the downstream of the turbine nacelle.

Figure 8c, d shows the measured TKE and Reynolds shear stress distributions in the wake of the wind turbine model. It can be seen clearly that, corresponding to the shedding of the unsteady tip vortices in the wake flow, the TKE levels along the shedding path of the tip vortex structures were found to be quite high. The wake flow downstream of the turbine nacelle was also found to be highly turbulent (i.e., with very high TKE). The high TKE levels in the regions are believed to be closely related to the generation of the unsteady root vortices and flow separation around the turbine nacelle, as revealed clearly from the
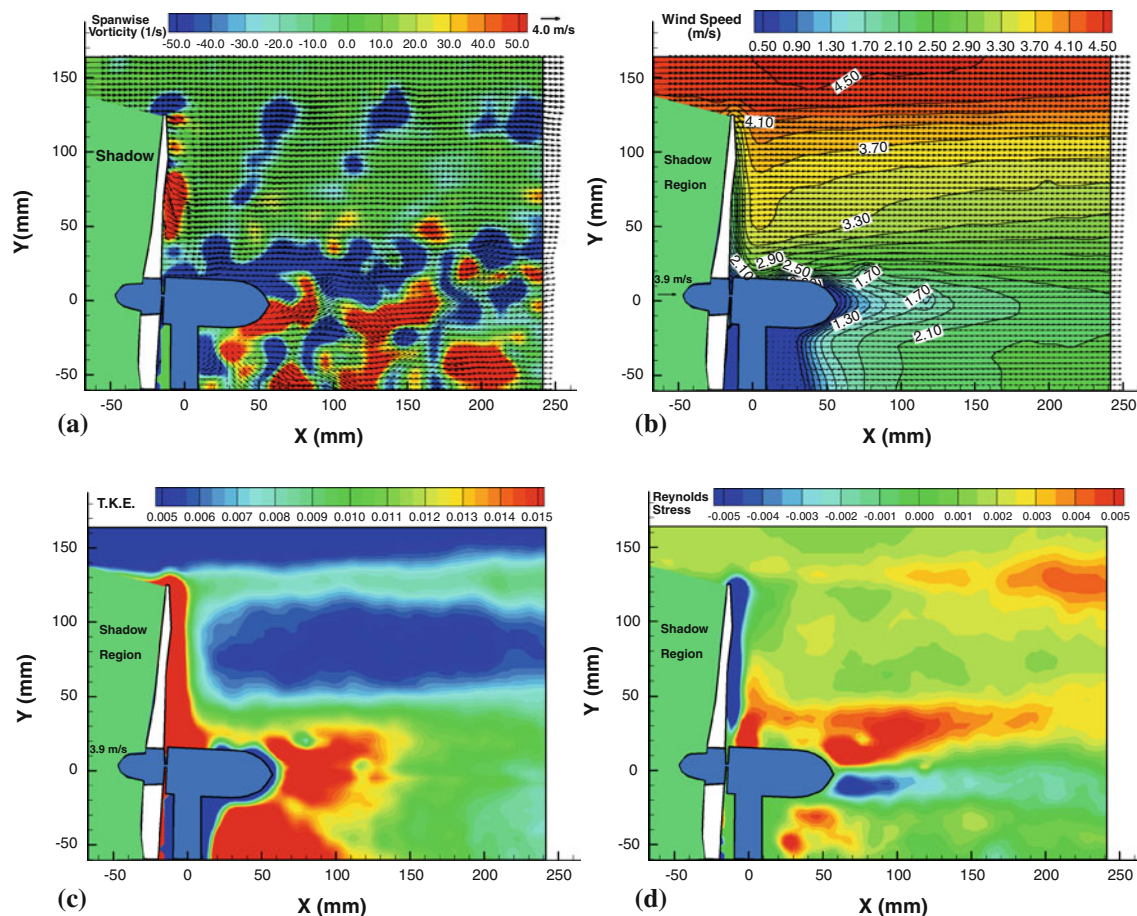
Fig. 8 PIV measurement results at the tip-speed-ratio of $\lambda = 3.0$. **a** Instantaneous PIV results. **b** Ensemble-averaged PIV results. **c** Turbulent kinetic energy distribution. **d** Reynolds stress distribution

instantaneous PIV measurement results. Turbulent vortex structures were also found to appear in the wake of the turbine tower, via shedding unsteady Karman vortices. As shown in Fig. 8, the high TKE levels in the region under the turbine nacelle could be attributed to the interference between the turbulent wake flow of the turbine tower and unsteady vortex structures induced by the rotating turbine blades.

As revealed clearly from the measured Reynolds stress distribution given in Fig. 8d, the regions with high levels of the Reynolds shear stress were found to concentrate in the shedding paths of the tip vortices and the root vortex structures as well as in the wake regions downstream of the turbine nacelle and tower. As suggested by Cal et al. (2010), the high Reynolds stress in the wake of a wind turbine would play an important role in promoting the vertical transport of the kinetic energy in the wake of the wind turbine, which will draw down more high velocity wind from above to the boundary layer flow, resulting in a fast recovery of the velocity deficit in the wake of a wind turbine. The findings revealed from the PIV measurement results are found to agree well with the observations

of Chamorro and Porte-Agel (2009), who conducted flow measurements by using a pointwise cross-wire anemometer.

In the present study, the effects of the tip-speed-ratio of the wind turbine model on the flow characteristics in the wake of the wind turbine model were also examined. Figure 9 shows the ensemble-averaged PIV measurement results with the tip-speed-ratio of the turbine model changing from $\lambda = 3.0$ to $\lambda = 4.5$. While the PIV measurement results reveal a very similar wake flow pattern, some obvious differences can still be identified from the comparison of the plots at different tip-speed-ratios. It can be seen clearly that, as the airflow passes the rotation disk of the turbine blades, the velocity deficits in the wake region (i.e., the loss of the kinetic energy) were found to be much smaller for the cases with relatively high tip-speed-ratios (i.e., for the cases of $\lambda = 4.0$ or $\lambda = 4.5$) compared with those with relatively low tip-speed-ratios (i.e., the cases of $\lambda = 3.0$ or $\lambda = 3.5$). It indicates that wind turbine could harvest much less wind energy if the tip-speed-ratio of the wind turbine model was too high, which confirmed the analysis described above and shown schematically in Fig. 7.
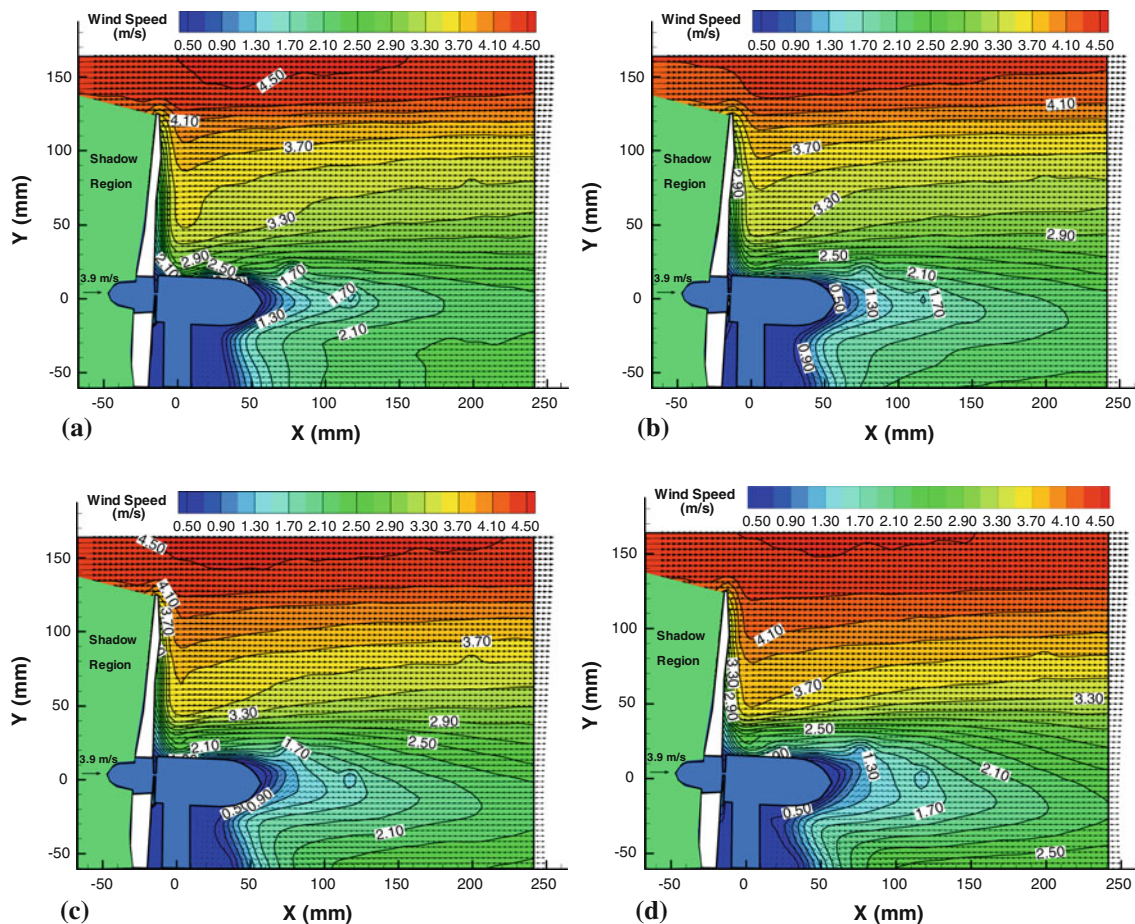
Fig. 9 Ensemble-averaged PIV measurement result at different tip-speed-ratios. **a** $\lambda = 3.0$, **b** $\lambda = 3.5$, **c** $\lambda = 4.0$, **d** $\lambda = 4.5$

In order to elucidate the effects of the tip-speed-ratio of the wind turbine more clearly and quantitatively, the transverse profiles of the ensemble-averaged wind speed and the TKE at the downstream location of $X/R = 1.0$ as a function of the tip-speed-ratio of the wind turbine model are shown in Fig. 10. The mean velocity profile of the incoming atmospheric boundary layer wind was also plotted in the figure for comparison. It can be seen clearly that, compared with the velocity profile of the incoming airflow, significant velocity deficits were found to be generated in the wake flow due to the installation of the wind turbine model in the atmospheric boundary layer wind. The size of the regions with significant velocity deficits were found to be much greater than that can be expected from the turbine nacelle only. It indicates that the incoming airflow would be decelerated greatly as they pass through the rotation disk of the turbine blades. According to the momentum and energy conservation laws, while the aerodynamic drag force acting on the wind turbine is proportional to the square of the velocity deficits, the power output of the wind turbine model (i.e., the wind energy harvested by the wind turbine model) would be

proportional to the cube of the velocity deficits. Larger velocity deficits in the transverse velocity profiles would indicate stronger aerodynamic loads acting on the wind turbine model as well as more wind energy harvested by the wind turbine model. As revealed from the transverse mean velocity profiles shown in Fig. 10, the largest velocity deficit in the wake flow was found at the tip-speed-ratio $\lambda \approx 3.0$ for the present study. It would suggest that the wind turbine model would experience the maximum wind loads as well as have the best wind energy harvesting capability when it was operated at the tip-speed-ratio of $\lambda \approx 3.0$. The finding was confirmed quantitatively from the independent wind load measurement results given in Fig. 6. The normalized TKE profiles shown in Fig. 10b also revealed clearly that the wake flow downstream of the turbine nacelle would be highly turbulent (i.e., with very high TKE levels), corresponding to the shedding of the unsteady root vortex structures and flow separation around the turbine nacelle as revealed clearly from the PIV measurement results described above. A region with high turbine kinetic energy levels can also be found along the shedding path of the tip vortices in the wake of the wind

Fig. 10 Transverse profiles of the wake flow at the downstream location of $X/R = 1.0$. **a** Time-averaged velocity profiles. **b** Normalized turbulence kinetic energy profiles
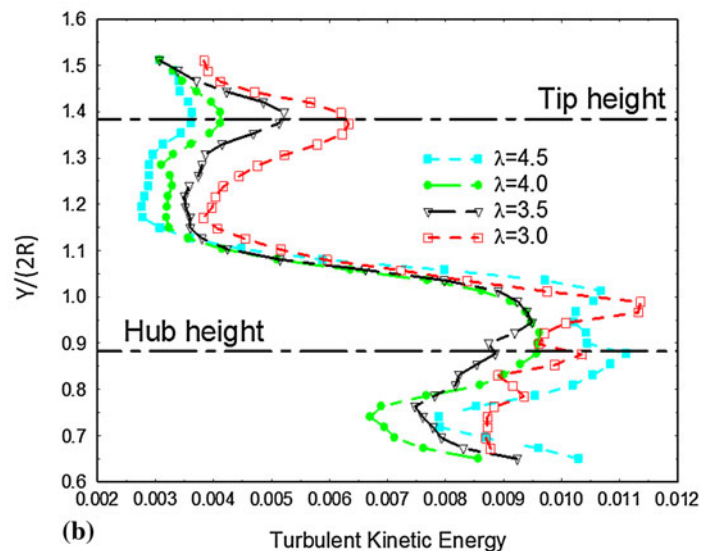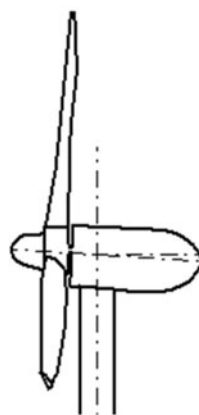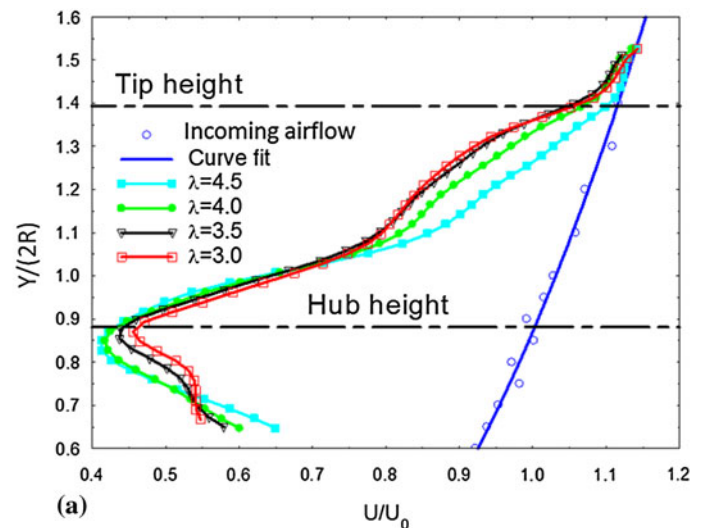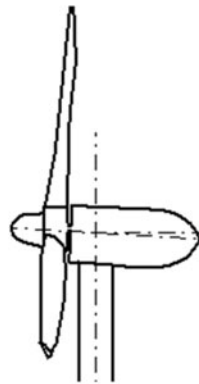
turbine model. The high turbulence level in the wake flow would indicate a highly unsteady wind loads acting on the wind turbine model, which would affect the mechanical strength and fatigue lifetime of the wind turbine model significantly. The findings derived from the present study are found to agree well with the observations of Chamorro and Porte-Agel (2009).

3.3 Phase-locked PIV measurement results

"Phase-locked" PIV measurements were conducted to produce "frozen" images of the unsteady wake vortex structures at different phase angles, from which the evolution of the unsteady wake vortex structures can be revealed more clearly and quantitatively. In the present study, the angle between the vertical PIV measurement plane and the position of a pre-marked rotor blade (i.e.,

blade #1) is defined as the phase angle. Figure 11 shows the phase-locked PIV measurement results with the tip-speed-ratio of the wind turbine model being $\lambda = 3.0$ and phase angle changing from 0° to 120°. As shown in the figures, the pre-marked turbine blade would be in the most upward position (i.e., within the vertical PIV measurement plane) at the phase angle of $\theta = 0°$. As the phase angle increases, the turbine blade would rotate out of the vertical PIV measurement plane. The second turbine blade would rotate into the PIV measurement plane at the phase angle of $\theta = 120°$. One of the obvious flow features that can be identified from the "phase-locked" PIV measurements is the existence of "wave-shaped" flow structures at the tip height of the wake flow, which were found to propagate downstream as the phase angle increases. The generation of "wave-shaped" flow structures is actually due to the periodic shedding of the tip vortex structures, which are
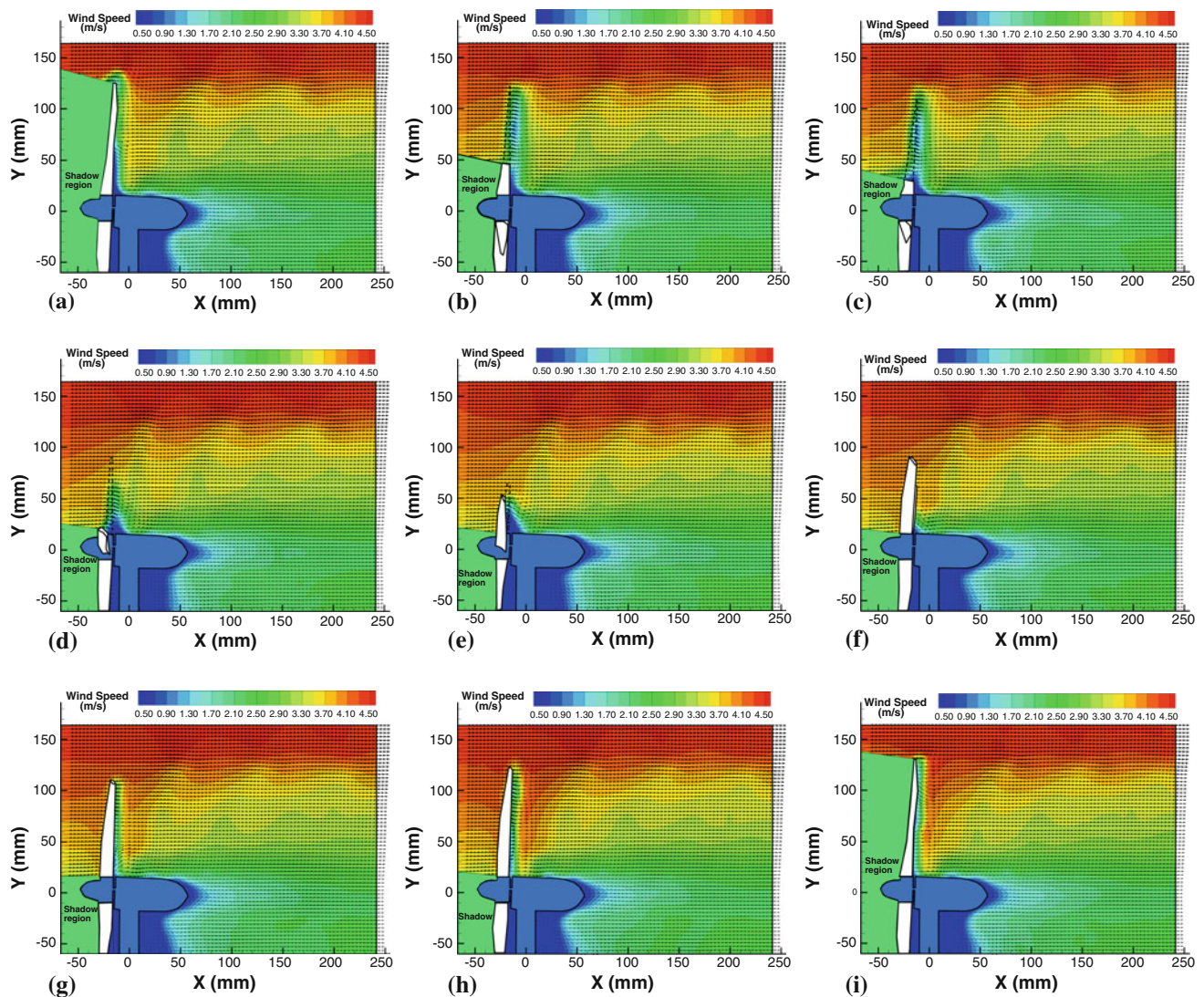
Fig. 11 "Phase-locked" PIV measurement results at the tip-speed-ratio of $\lambda = 3.0$. **a** $\theta = 0.0°$, **b** $\theta = 15°$, **c** $\theta = 30.0°$, **d** $\theta = 45°$, **e** $\theta = 60°$, **f** $\theta = 75°$, **g** $\theta = 90°$, **h** $\theta = 105°$, **i** $\theta = 120°$

revealed more clearly in Fig. 12 and will be discussed in detail later. It can also be seen that, as the phase angle increases (i.e., as the pre-marked turbine blade was rotating out of the PIV measurement plane), high-speed airflows (i.e., the region with red color contour) would intrude more deeply down into the boundary layer flow in the region downstream of the rotation disk of the wind turbine model. It indicates that the wind energy of the airstreams within the PIV measurement plane would be harvested only when the turbine blades were rotated into the plane, as expected. Similar findings were also reported in the study of Massouh and Dobrev (2007).

Figure 12 shows the vorticity distributions in the wake of the wind turbine model, which were derived from the "phase-locked" PIV measurements at different phase angles, in order to reveal the evolution of the unsteady

wake vortex structures more clearly. As described above, the pre-marked turbine blade would be within the vertical PIV measurement plane at the phase angle of $\theta = 0°$. It can be seen clearly that a tip vortex would be induced at the tip of the pre-marked turbine blade at $\theta = 0°$. As the phase angle increases, while the pre-marked turbine blade would rotate out of the vertical PIV measurement plane, the tip vortex was found to shed from the tip of the turbine blade and move downstream, as indicated by the red dashed line in the figure. It can also be seen that the tip vortex induced by the pre-marked blade (i.e., the 1st blade) would align itself nicely with the other tip vortices induced by the 2nd and 3rd turbine blades to form a moving tip vortex array in the wake flow. The relative velocity vectors (i.e., after subtracting the velocity of the incoming airflow at the tip height of the turbine blade from the measured flow velocity

Fig. 12 Evolution of the tip vortex structures at the tip-speed-ratio of $\lambda = 3.0$
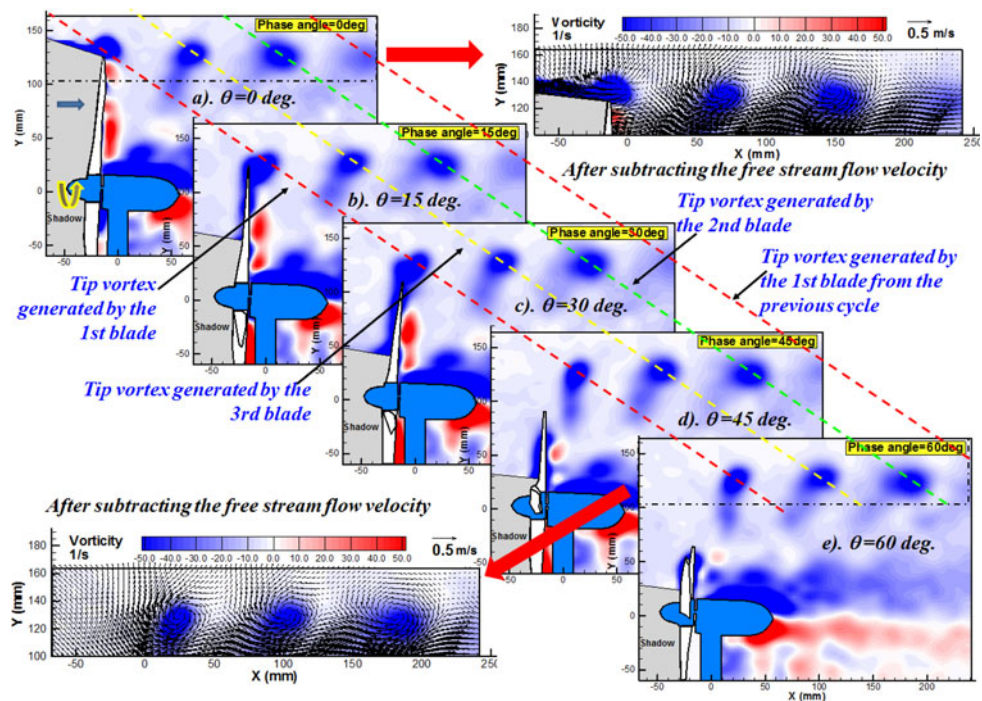
fields) at phase angle $\theta = 0°$ and $\theta = 60°$ were also given in the figure in order to visualize the formation and evolution of the tip vortex array more clearly. It can be seen clearly that the periodic shedding of the tip vortex array would cause the formation of "wave-shaped" structures at the tip height, as shown clearly in the "phase-locked" PIV measurement results given in Fig. 11. It should also be noted that, in addition to the tip vortex array, the periodic shedding of the unsteady vortex structures at the roots of the rotating blades and the flow separation around the turbine nacelle were also visualized clearly from the "phase-locked" PIV measurement results.

It should be noted that the PIV measurement results presented above represents only a plane view of a complex 3-D wake vortex flow within the vertical measurement plane. It is highly desirable and much more effective to elucidate underlying physics if a 3-D view of the wake vortex flow can be reconstructed. In the present study, a 3-D view of the wake vortex structures in the wake of the wind turbine model was reconstructed based on the "phase-locked" PIV measurement results, which is shown in Fig. 13. The trajectories of the tip vortex structures, which were determined by tracking the centers of the tip vortices induced by the three turbine blades at different phase angles, were added in the figure in order to elucidate the helical motion of the tip vortices more clearly. It can be seen clearly that the tip vortices originated from the tips of the rotor blades would form three helical vortex tubes as they moved downstream. The helical motion of the tip vortices was found to be reverse to the rotation direction of
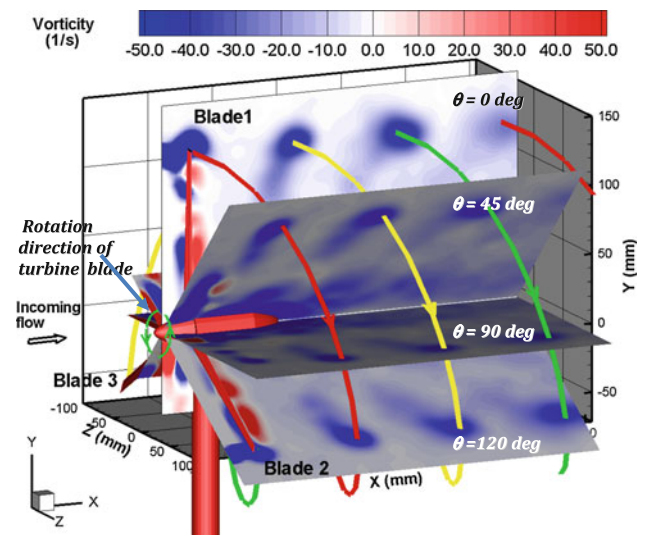

Fig. 13 A 3-D view of the tip vortex structures in near wake of the wind turbine model

the turbine blades. The gap between the helical vortex tubes was found to be a function of the tip-speed-ratio of the wind turbine model, which can be seen more clearly in Fig. 15. While the helical tip vortex structures in the wakes of wind turbines were visualized qualitatively with smoke in previous studies (Anderson et al. 1982; Vermeer 2001; Hand et al. 2001), the 3-D view of the PIV measurement results given in the present study is believed to be the first to elucidate the formation and evolution of the helical tip vortex structures quantitatively.
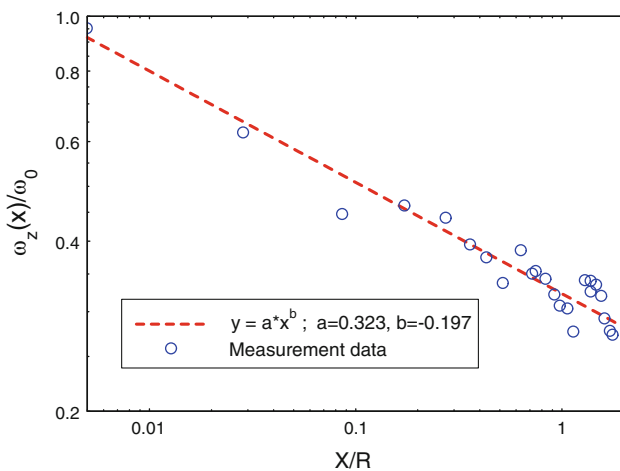
Fig. 14 The strength decay of the tip vortices versus downstream distance at $\lambda = 3.0$

The strength of the helical tip vortices, which can be determined quantitatively based on the "phase-locked" PIV measurements, was also found to change significantly as they moved downstream. Figure 14 shows the decay

profile of the peak vorticity of the tip vortices with the wind turbine model operating at the tip-speed-ratio of $\lambda = 3.0$. The measurement data shown in the figure were obtained by tracking the maximum vorticity of the tip vortices revealed from the "phase-locked" PIV measurement results at different phase angles. It can be seen clearly that the strength of the tip vortices would decay rapidly as they travelled downstream. The tip vortex structures were found to have only about 35% of their original strength as they travelled to the downstream location of $X/R = 1.0$. As shown in the figure, the strength decay profile of the tip vortices can be fitted well by using a power law function. It indicates that the strength of the tip vortices would decay rapidly following a power law in the near wake of the wind turbine model.

Figure 15 shows the typical "phase-locked" PIV measurement results with the wind turbine model operating at four different tip-speed-ratios. The effects of the tip-speed-ratio of the wind turbine model on the evolution of the unsteady vortex flow structures in the wake of the wind turbine model were revealed clearly from the comparison of the PIV measurement results. It can be seen clearly that
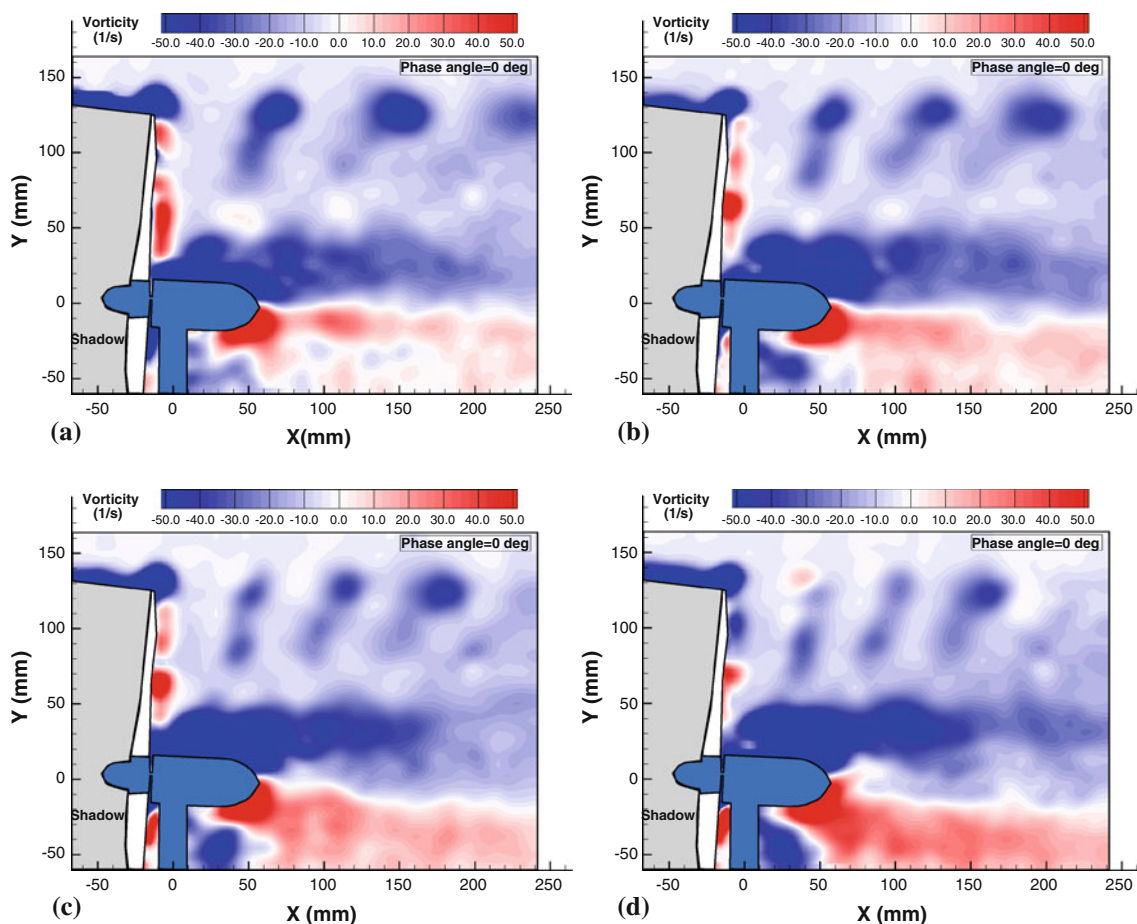

Fig. 15 The evolution of the wake vortex structures at difference tip-speed-ratios. **a** $\lambda = 3.0$, **b** $\lambda = 3.5$, **c** $\lambda = 4.0$, **d** $\lambda = 4.5$

the distance between the neighboring tip vortices (i.e., the pitch gap between the helical tip vortex tubes as shown in Fig. 13) would decrease almost linearly as the tip-speed-ratio of the wind turbine model increases. The strength of the tip vortices was found to become much weaker as the wind turbine model operated at a higher tip-speed-ratio. This observation is believed to be closely related to the formation mechanism of the tip vortices. It is well known that the generation of tip vortices is due to the pressure differences between the pressure and suction sides of the wind turbine blades. As the tip-speed-ratio of the wind turbine model increases, the effective angle of attack of the incoming airflow with respect to the airfoil cross-section would become smaller and smaller, as illustrated in Fig. 7. The smaller pressure difference between the pressure and suction sides of the turbine blades at smaller effective angles of attack would result in weaker tip vortices, as revealed clearly in Fig. 15. It can also be found that the unsteady vortices shedding from the roots of the turbine blades and turbine nacelle would become much bigger and stronger as the tip-speed-ratio increases. As a result, the flow separation regions around the turbine nacelle were found to increase with the increasing tip-speed-ratio of the wind turbine model, as revealed clearly in the time-averaged PIV measurement results shown in Fig. 9. It should also be noted that the additional row of the unsteady vortex structures shedding at approximately 50–60% span of the turbine blades were found to become more distinct for the cases with higher tip-speed-ratio, while they were still found to merge with the tip vortex structures at further downstream.

As described above, while the strength of the tip vortices was found to decay rapidly in the wake of the wind turbine model, the tip vortices were also found to wander around as they travelled downstream. Figure 16 shows the instantaneous center positions of the tip vortices in the wake of the wind turbine model, which were derived from 100 instantaneous frames of "phase-locked" PIV measurement results at the same phase angle of $\theta = 0°$. The phase-averaged trajectory lines of the helical tip vortex tubes were also shown in the plots for reference. The wandering feature of the tip vortices was revealed clearly from the scatterings of the instantaneous center positions of the tip vortices at different time instances (i.e., different rotation cycles) but with the same phase angle of $\theta = 0°$. It should be noted that, while the instantaneous centers of the tip vortices were found to be wandering around their phase-averaged centers randomly, further data reduction reveals that the probability density function (pdf) of the instantaneous locations of the tip vortex centers could be represented well by using Gaussian functions. The wandering range of the tip vortices were indicated by the circles plotted in the figures. It can be seen clearly that the wandering range of the tip vortices would become larger and larger as they moved further away from the turbine blade tips. The larger wandering range of the tip vortices at further downstream locations is believed to be closely related to the weaker strength of the tip vortices and higher TKE level of the wake flow in those locations, as revealed clearly and quantitatively from the PIV measurement results given above.

Based on the comparison of the test cases with the tip-speed-ratio of the wind turbine model at $\lambda = 3.0$ and $\lambda = 4.0$, it can be seen clearly that the tip-speed-ratio of the wind turbine model would have observable effects on the wandering of the tip vortices in the wake flow. The wandering of the tip vortex structures was found to become less pronounced as the tip-speed-ratio of the wind turbine model increases. As shown in Fig. 16, at the same downstream location of $X/R \approx 2.0$, the wandering range was found to be about 40 mm for the test case with the tip-speed-ratio of $\lambda = 3.0$, while the wandering range was found to become only about 30 mm for the case with the
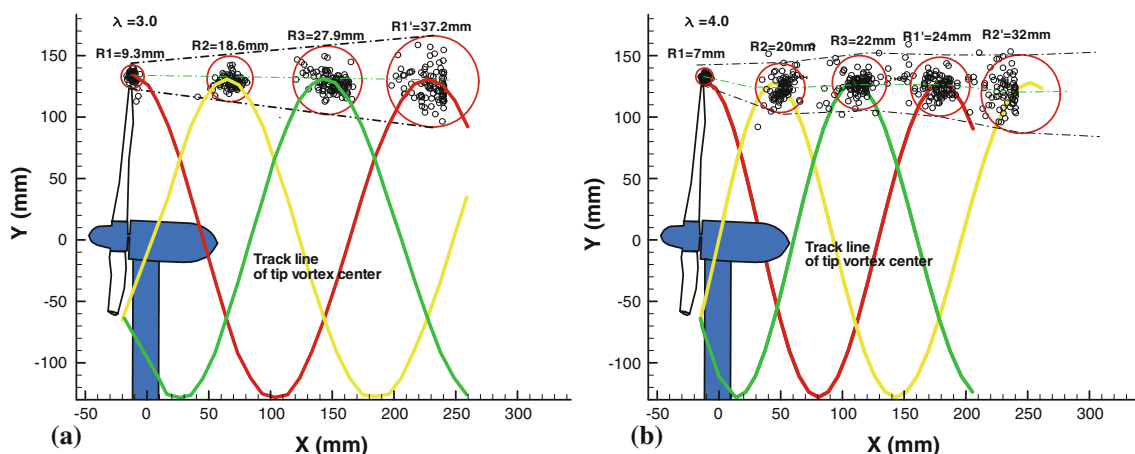

Fig. 16 The wandering of the tip vortices at different tip-speed-ratios. a $\lambda = 3.0$, b $\lambda = 4.0$

tip-speed-ratio of $\lambda = 4.0$. The wandering of the tip vortex structures is believed to be closely related to the turbulence characteristics of the atmospheric boundary layer winds as well as the wake meandering as investigated by Bingol et al. (2007) and Larsen et al. (2008).

4 Conclusion

A wind tunnel study was conducted to quantify the unsteady wind loads acting on a HAWT model and the evolution of the turbulent vortex structures in the near wake of the wind turbine model. In addition to measuring dynamic wind loads acting on the wind turbine model by using a high-sensitive force-moment sensor, a high-resolution PIV system was used to make both "free-run" and "phase-locked" measurements to quantify the flow characteristics in the near wake of the wind turbine model.

The measurement results reveal clearly that, while the instantaneous wind loads (i.e., both aerodynamic forces and bending moments) acting on the wind turbine model would be highly unsteady with their magnitudes being about 2–3 times greater than the time-averaged values, the histograms of the dynamic wind loads were found to be fitted reasonably well by using Gaussian functions. The wind loads acting on the wind turbine model were found to increase with the increasing tip-speed-ratio at first, reach their peak values at the tip-speed-ratio of $\lambda \approx 3.0$, and then decrease gradually at $\lambda > 3.0$ for the present study. The variations of the resultant flow velocity and effective angle of attack of the incoming airflow related to the turbine blade at different tip-speed-ratios were used to qualitatively explain the wind load measurement results.

"Free-run" PIV measurements were conducted to determine the ensemble-averaged flow statistics (e.g., mean velocity, Reynolds Stress, and TKE) in the near wake of the wind turbine model. It was found that incoming airflow would be decelerated rapidly passing through the rotation disk of the turbine blades. The largest velocity deficits of the wake flow were found to occur at the tip-speed-ratio of $\lambda \approx 3.0$. It implies that the wind turbine model would experience the maximum wind loads as well as have the best wind energy harvesting capability when it operated at the tip-speed-ratio of $\lambda \approx 3.0$ for the present study, which was confirmed by the independent wind load measurements. As expected, the regions with high TKE and Reynolds stress levels were found to concentrate in the regions along the shedding paths of the unsteady tip vortices and root vortex structures as well as the wake regions downstream of the turbine nacelle and tower. The findings revealed from the PIV measurements were found to agree well with the observations of previous studies based on pointwise hotwire anemometer or/and LDV measurements.

The evolution of the unsteady vortex and turbulence flow structures in the wake of the wind turbine model in relation to the position of the rotating rotor blades were elucidated clearly from the "phase-locked" PIV measurements. It was found that the tip vortices would form three helical vortex tubes in the wake flow as they travelled downstream. The helical motion of the tip vortex tubes was found to be reverse to the rotation direction of the turbine blades. The tip-speed-ratio of the wind turbine was found to have significant effects on the evolution of the tip vortex structures. While the gap between the helical tip vortex tubes was found to decrease almost linearly with the increasing tip-speed-ratio of the wind turbine, the tip vortices were found to become much weaker as the wind turbine model operates at higher tip-speed-ratios. The unsteady vortices shedding from the roots of the turbine blades and turbine nacelle were found to become bigger and stronger as the tip-speed-ratio of the wind turbine model increases. The strength of the tip vortices was found to decay rapidly following a power law in the near wake of the wind turbine model. The tip vortices were also found to wander around as they travelled downstream. The wandering range of the tip vortices was found to become larger and larger as they moved further away from the rotation disk of the turbine blades. The wandering of the tip vortices is believed to be closely related to the high turbulence levels of the atmospheric boundary layer winds and could also be linked to the wake meandering phenomena reported in previous studies.

References

Alfredsson PH, Dahlberg JA (1979) A preliminary wind tunnel study of windmill wake dispersion in various flow conditions. Technical note AU-1499, part 7, FFA, Stockholm

Alfredsson PH, Dahlberg JA, Vermeulen PEJ (1982) A comparison between predicted and measured data from wind turbine wakes. Wind Eng 6(3):149–155

American Society of Civil Engineering (2005) ASCE 7-05 minimum design loads for building and other structures, ASCE

Anderson MB, Milborrow DJ, Ross NJ (1982) Performance and wake measurements on a 3 m diameter horizontal axis wind turbine: comparison of theory, wind tunnel and field test data. Technical report, Department of Physics, University of Cambridge

Architecture Institute of Japan (1996) AIJ recommendations for loads on buildings, AIJ

Bingol F, Larsen GC, Mann J (2007) Wake meandering—an analysis of instantaneous 2D laser measurements. J Phys Conf Ser 75:012059

Boeing (1982) Mod-2 wind turbine system development final report, vol II detailed report, nASACR-168007, DOE/NASA/0002-82/2. NASA Lewis Research Center, Cleveland

Cal R, Lebron J, Castillo L, Kang H, Meneveau C (2010) Experimental study of the horizontally averaged flow structure in a model wind-turbine array boundary layer. J Renew Sustain Energy 2:013106

Chamorro LP, Porte-Agel F (2009) A wind-tunnel investigation of wind-turbine wakes: boundary layer turbulence effects. Bound Layer Meteorol 132:129–149

Ebert PR, Wood DH (1997) The near wake of a model horizontal-axis wind turbine: part 1: experimental arrangements and initial results. Renew Energy 2:225–243

Grant I, Parkin PA (2000) DPIV study of the trailing vortex elements from the blades of a horizontal axis wind turbine in yaw. Exp Fluids 28:368–376

Hand MM, Simms DA, Fingersh LJ, Jager DW, Cotrell JR, Schreck S, Larwood SM (2001) Unsteady Aerodynamics Experiment Phase VI: wind tunnel test configurations and available data campaigns. National Renewable Energy Laboratory, Golden, CO, NREL/TP-500-29955

Jain P (2007) Wind energy engineering. McGraw Hill. ISBN:978-0-07-171477-8

Larsen GC, Madsen HA, Thomsen K, Larsen TJ (2008) Wake meandering: a pragmatic approach. Wind Energy 11:377–395

Massouh H, Dobrev I (2007) Exploration of the vortex behind of wind turbine rotor. J Phys Conf Ser 75:012036

Medici D, Alfredsson PH (2006) Measurements on a wind turbine wake: 3D Effects and bluff body vortex shedding. Wing Energy 9:219–236

Schreck S, Lundquist J, Shaw W (2008) U. S. Department of Energy workshop report: research needs for wind resource characterization. National Renewable Energy Laboratory technical report, NREL/TP-500-43521

Spera AD (1994) Wind turbine technology. ASME Press, New York, pp 219–220

Tsustui Y, Matsumya H (1987) LDV measurements of flow field around a wind turbine. Wind Power 381–386

Vermeer LJ (2001) A review of wind turbine wake research at TU-Delft. A collection of the 2001 ASME wind energy symposium technical papers. ASME, New York, pp 103–113

Vermeer LJ, Sorensen JN, Crespo A (2003) Wind turbine wake aerodynamics. Prog Aerosp Sci 39:467–510

Whale J, Anderson CG, Bareiss R, Wagner S (2000) An experimental and numerical study of the vortex structure in the wake of a wind turbine. J Wind Eng Ind Aerodyn 84:1–21